frontiers in Energy Research

ORIGINAL RESEARCH
published: 27 January 2021
doi: 10.3389/fenrg.2020.606237

Carbon-Interlayer SnO_2–Sb_2O_3 Composite Core–Shell Structure Anodes for Sodium-Ion Batteries

Guoju Zhang[1], Yuanduo Qu[2], Fanghui Zhao[1], Rongxin Dang[1], Jie Yang[1], Liying Wang[1], Yuanpeng Zhang[1] and Lianfeng Duan[2]**

[1]Key Laboratory of Advanced Structural Materials, Ministry of Education, and School of Materials Science and Engineering, Changchun University of Technology, Changchun, China, [2]Department of Chemistry, Shantou University, Shantou, China

Although great efforts have been dedicated to improving electrochemical property of oxides anode material for sodium-ion batteries, the cycling life and rate capability of oxides anode materials are still far from its theoretical value. Herein, novel uniform SnO_2@C@Sb_2O_3 submicrospheres with multilayer core–shell hollow structure have been synthesized as anode of sodium-ion batteries. The multilayer core–shell structure SnO_2@C@Sb_2O_3 composite delivers a reversible capacity of 269 mAh g^{-1} at higher current density (1,500 mA g^{-1}) after 100 cycles and exhibited excellent rate performance. The conductivity of the anode composite is promoted by the uniformly carbon dispersion through the whole submicrospheres. The dramatic volume change of electrode material could be mitigated by the porous core–shell structure of Sb_2O_3 and SnO_2 during charge–discharge process. The enhanced specific capacity and rate performance are mainly ascribed to the integrity of structure and synergy effect between different metal oxides.

Keywords: metal oxides (mixed), core–shell structure, sodium-ion batteries, anodes, carbon-interlayer

OPEN ACCESS

Edited by:
Daniel Q. Tan, Technion Israel Institute of Technology, Israel

Reviewed by:
Liqiang Mai, Wuhan University of Technology, China
Zhenjiang He, Central South University, China

****Correspondence:***
Liying Wang
wangliying@ccut.edu.cn
Lianfeng Duan
duanlf2011@sina.cn

Specialty section:
This article was submitted to Electrochemical Energy Conversion and Storage, a section of the journal Frontiers in Energy Research

Received: *14 September 2020*
Accepted: *24 November 2020*
Published: *27 January 2021*

Citation:
Zhang G, Qu Y, Zhao F, Dang R, Yang J, Wang L, Zhang Y and Duan L (2021) Carbon-Interlayer SnO_2–Sb_2O_3 Composite Core–Shell Structure Anodes for Sodium-Ion Batteries. Front. Energy Res. 8:606237. doi: 10.3389/fenrg.2020.606237

INTRODUCTION

The energy storage systems, especially for Li-ion batteries (LIBs), are increasingly important in commercial 3C (computer, communication, and consumer electronic) products, and new standards have been defined in the fields of electric/hybrid vehicles and industries with storage energy (Tarascon and Armand, 2001). As alternatives to LIBs, many attentions have been paid on the new energy storage devices (Shan et al., 2019), especially for sodium-ion batteries (SIBs), because of their similar potential closed to Li^+ and lower cost (Eguia-Barrio et al., 2017). The demand of stable electrode materials with low cost was mainly focused on various compounds, such as $Na_3V_2(PO_4)_3$, $Na_{1.25}V_3O_8$, and $NaCrO_2$ for cathode materials (Kim et al., 2012). Among SIB anode materials, many kinds of composites such as alloy, metal oxide, and metal sulfide with carbon as the substrate have become the research focus (Luo et al., 2016).

For anode materials with alloying reactions, such as Sb and Sn alloy, even the relatively low redox potential provides high voltage for a full cell (Wang et al., 2016). Unfortunately, this huge volume change (420% volume expansion in the process of forming $Na_{15}Sn_4$) resulting in serious pulverization of active materials and fast capacities fade of electrode (Zhu et al., 2013; Wang et al., 2014). Changes in volume make the electrode material more vulnerable to structural damage (Dong et al., 2018), which is an intrinsic drawback that limits the use of many anode materials in SIBs. Different from the alloy materials, the intermetallic and metal oxides with high gravimetry- and

volumetry-specific capacities have been studied widely. Their reversible redox reactions are based on the conversion reactions of Na_2X (X = O, P, S, etc.), which can relieve the stress of large volume change and contribute to a better electrode chemical performance. Among tin-based compounds investigated as electrode materials, SnO_2 has received a special attention, owing to a high theoretical reversible specific capacity (667 mAh g^{-1}), environmental benignity, and quite low cost (Morita et al., 2016; Zhang et al., 2017; Lee et al., 2018). However, low conductivity and high redox potential suppressed the practical use of SIBs.

In recent, it has drawn increasing attentions for-alloy type anodes with core–shell nanoporous structures and carbon-based composites due to their adjustable space for volume expansion (Wang et al., 2012; Xu et al., 2016). It is reported that the prepared nanoporous CuSi and CuSn alloy anodes, and hollow spheres of metal oxide with large surface area provide enough place to suppress the structural damage (Bang et al., 2012; Ma et al., 2016; Chen et al., 2017). As SIB anode, SnO_2 and SnO_2@graphene nanocomposite delivered 432 mAh g^{-1} after 150 cycles and 638 mAh g^{-1} after 100 cycles, respectively (Liu et al., 2010; Su et al., 2013b). Wu et al. reported the Sn–SnS–C nanocomposites with the reversible ability of 664 mAh g^{-1} at 20 mA g^{-1} and 350 mAh g^{-1} at 800 mA g^{-1} as SIB anodes (Wu et al., 2013). Furthermore, the introduction of metal elements can improve sluggish reaction kinetics, and the synergistic effects of multi-metal led to improve the structural stability and reduce the capacity density loss as much as possible (Rui et al., 2014; Su et al., 2014). Thus, environmentally friendly and resourceful compound metal dioxide with special structure has been increasing attention for their wide applications in energy storage (Sun et al., 2006; Zhu et al., 2013; Wang et al., 2014). Therefore, it is of great significance to develop a carbon-based multi-metal composite with core–shell nanoporous for improving the electrochemical performance of SIBs.

In this article, the SnO_2@C@Sb_2O_3 with core–shell nanoporous is designed and synthesized for improving the performance of SIBs. SnO_2 provides enough capacity, as a metallic core with the plenty of nanopores. The carbon shell not only improves the overall conductivity of the electrode material but also plays an important role in accommodating the volume change upon sodiation/disodiation. Furthermore, the Sb_2O_3 as the framework could be used for improving the structural stability and reducing the capacity density loss. It is realized that the successful utilization of anode composites to achieve excellent electrochemical performance in practical high-energy SIBs is based on the strategy of this facile and scale up material fabrication.

EXPERIMENTAL SECTION

Materials and Preparation

In this work, the composites were synthesized by the hydrothermal method. Glucose (0.5 g) was first dissolved in distilled water (35 ml), and then added 0.15 g $SnCl_4{\cdot}5H_2O$. The suspension was sonicated for 90 min. Then, 0.3 g $SbCl_3$ was added to the above solution and sonicated until the solution became relatively uniform. The mixture was then transferred into a 50-ml Teflon-sealed autoclave and maintained at 180°C for 12 h. The product was collected after being washed with deionized water and ethanol by centrifugation. Then, the product was vacuum-dried at 80°C for 24 h. In order to find the most suitable temperature for calcination, the sample was divided into four parts. The four parts were then respectively heated in muffle roaster at the rate of 3°C min^{-1} to 200, 300, 400, and 500°C for 3 h.

Characterization

The crystal structure was characterized by X-ray diffraction (XRD, SiemensD-5000) with a scanning angle (2θ) ranging from 15° to 90°. The morphology of the products was analyzed by transmission electron microscopy (TEM, JEOL 2100F) and scanning electron microscopy (SEM, Hitachi S4800), respectively. X-ray photoelectron spectroscopy (XPS) (Thermo Scientific, Waltham, MA, United States) was used to determine the composition of the sample. The Raman (HR + Evolution) test was used to verify the presence of carbon material peaks in the samples.

Electrochemical Tests

The 2,032 coin cells were assembled in an argon-filled glove box for measuring the electrochemical measurements of working electrode. The working electrode included active material, carboxyl methyl cellulose (CMC) binder, and Super P carbon black as a carbon additive in dilute styrene butadiene rubber (SBR) aqueous solution at a weight ratio of 7:2:1. The counter anode was sodium metal, and the separator was glass fiber GF/F (Whatman) filter. The electrolyte was 1 M $NaClO_4$ dissolved in ethylene carbonate (EC) and diethyl carbonate (DEC) (1:1 by volume). Galvanostatic charge–discharge measurements were tested based on a multichannel battery testing system (LAND CT2001A). Cyclic voltammetry (CV) was performed through an electrochemical workstation (CHI 760D).

RESULTS AND DISCUSSION

The morphology of the as-prepared SnO_2@C@Sb_2O_3 composites after sintering at 500°C is shown in **Figure 1**. In **Figure 1A**, it can be observed that the surface of the unsintered SnO_2@C@Sb_2O_3 composite is relatively smooth. **Figure 1B** shows the FESEM images of the as-prepared particles, which exhibit uniform submicrospheres in an average around 500 nm diameter, and dense mesoporous on the surface of the submicrospheres can be found. Importantly, it is clearly observed that SnO_2@C@Sb_2O_3 particles have a rough surface, which is formed by the Sb_2O_3 outer layer of the subspheres during calcination to form a loose, porous shell, providing a fast channel for the migration of sodium ions/electrons. The microstructure of SnO_2@C@Sb_2O_3 composite was further investigated by TEM, as shown in **Figures 1C,D**. According to the TEM images, SnO_2@C@Sb_2O_3 composite has the expected multilayer core–shell structure, with SnO_2 particle in

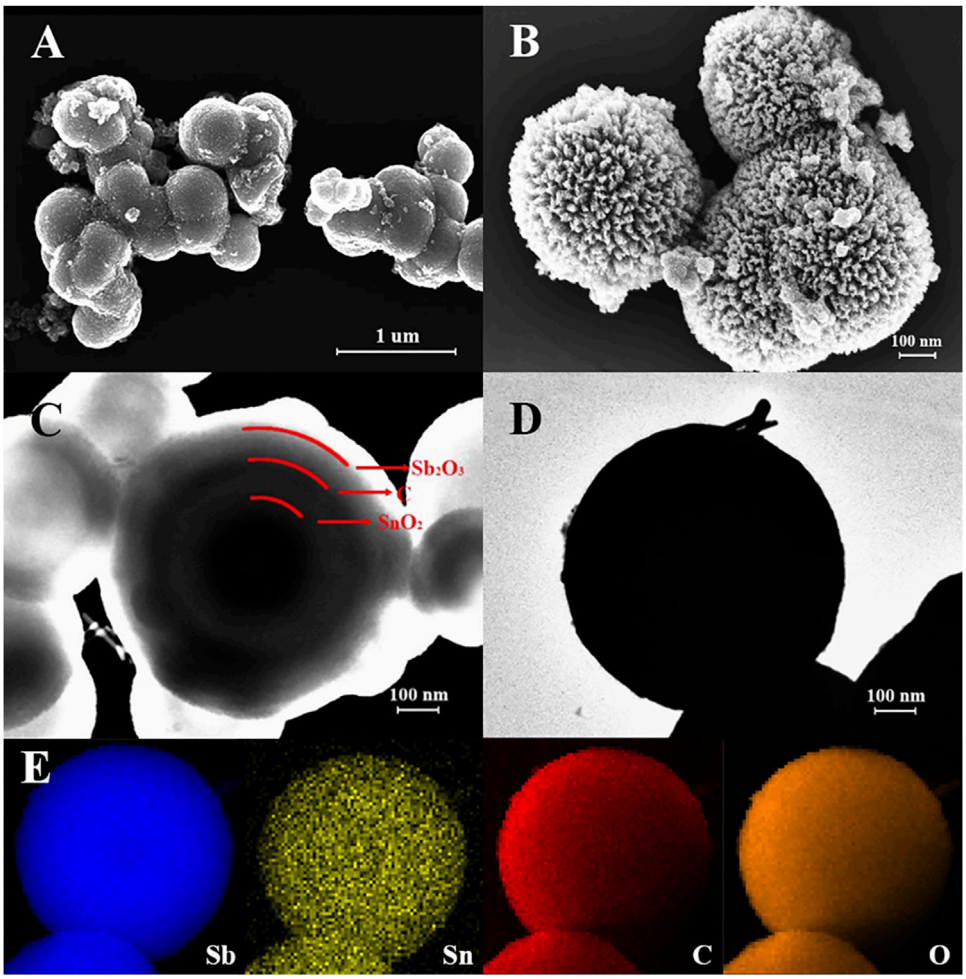

FIGURE 1 | (A) FSEM image of SnO_2@C@Sb_2O_3 submicrospheres without sintering; FSEM images of SnO_2@C@Sb_2O_3 multilayer core–shell submicrospheres after sintering at 500°C, **(B)** FESEM image, **(C,D)** TEM images, and **(E)** EDS elemental mapping images.

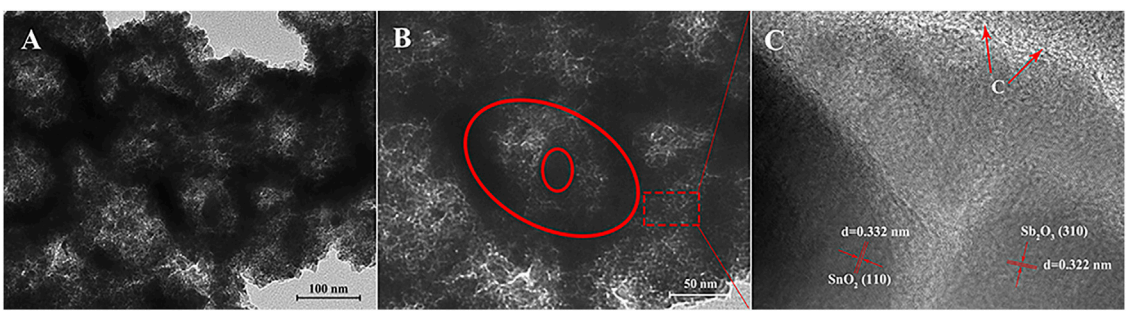

FIGURE 2 | (A,B) TEM and **(C)** HRTEM images of SnO_2@C@Sb_2O_3 submicrospheres at 500°C.

the innermost layer, carbon layer in the middle, and Sb_2O_3 shell in the outermost layer. It is clear that the three layers are separated from each other by hollow parts, which is conducive to adapt to the volume expansion of the core and the shell. The EDS elemental mapping of Sb, Sn, C, and O elements is shown in **Figure 1E**. All elements are evenly distributed to form a clear sphere, indicating that the core–shell structure is composed of SnO_2 and Sb_2O_3. And also, the carbon interlayer could be

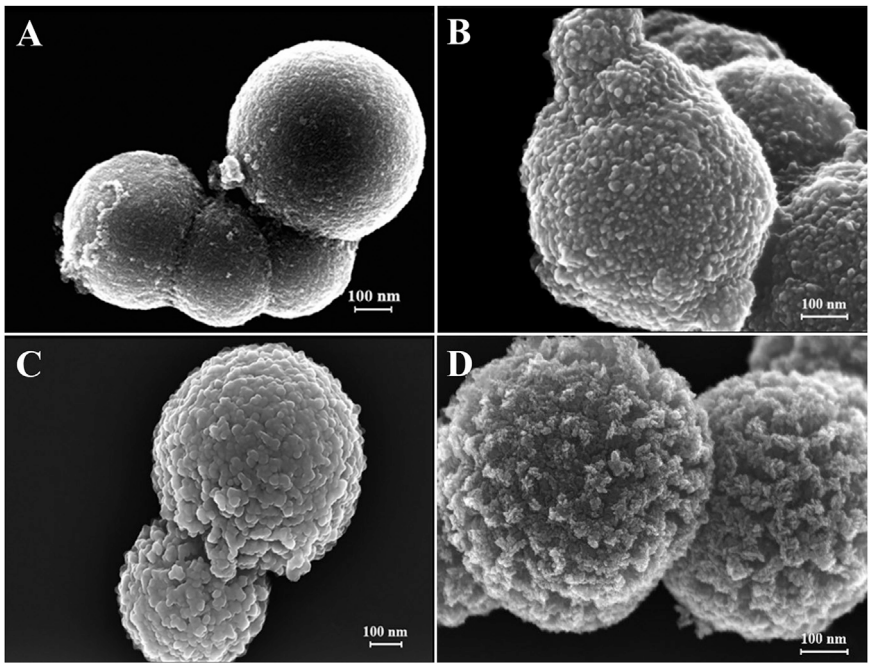

FIGURE 3 | FESEM images of SnO_2@C@Sb_2O_3 submicrospheres after sintering at different temperatures. **(A)** Without sintering, **(B)** 200°C, **(C)** 300°C, and **(D)** 400°C.

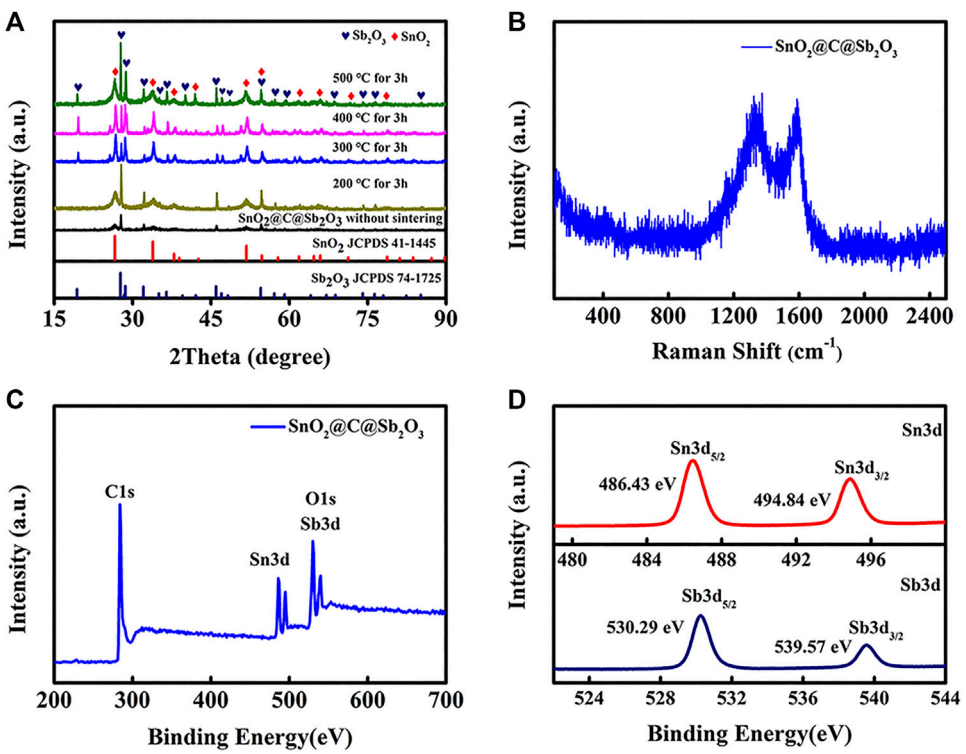

FIGURE 4 | (A) XRD patterns of the samples obtained with different sintering temperatures, **(B)** Raman spectra of SnO_2@C@Sb_2O_3, **(C)** XPS survey spectra of SnO_2@C@Sb_2O_3, and **(D)** high-resolution XPS spectra of Sn 3d and Sb 3d in SnO_2@C@Sb_2O_3.

introduced to the SnO_2–Sb_2O_3 composite with core–shell structure, which is consistent with the conclusion of **Figure 1C**.

Figure 2 shows the TEM and HRTEM images of the as-prepared SnO_2@C@Sb_2O_3 submicrospheres after sintering at 500°C. In **Figures 2A,B**, it is obvious that these submicrospheres have hollow and core–shell structures. Moreover, it is measured that the typical lattice fringe spacings as 0.322 and 0.332 nm (**Figure 2C**), which corresponds to the (310) crystal plane of Sb_2O_3 and the (110) crystal plane of SnO_2. The reason is that when the sintering temperature is 500°C, the inner solid core contracted sharply to form a hollow structure, resulting in a SnO_2, C, and Sb_2O_3 triple-shelled core–shell submicrosphere with a hollow structure. **Figure 3** presents the morphology of SnO_2@C@Sb_2O_3 composite without sintering (**Figure 3A**) and sintering at different heat treatment temperatures from 200 to 400°C (**Figures 3B–D**), respectively. The comparison results show that with the increase of heat treatment temperature, the Sb_2O_3 shell with smooth and dense surface on the submicrosphere becomes gradually sharp and loose. However, only when the heat treatment temperature increases to 500°C will the porous structure conducive to the diffusion of sodium ions/electrons be formed (**Figure 1B**).

The XRD patterns of the samples at different sintering temperatures are shown in **Figure 4A**. For the SnO_2@C@Sb_2O_3 composite without sintering, the characteristic peaks of SnO_2 and Sb_2O_3 are not strong as other sintered composites, which indicated that the crystallinity of the precursor prepared by hydrothermal method is not well. After the sintering of 200°C, the characteristic peak of the oxides has increased significantly, which are corresponding to Sb_2O_3 (JCPDS 74-1725) and SnO_2 (JCPDS 41-1445). With sintering temperature of the samples further increasing, it can be seen that the crystallization of the SnO_2@C@Sb_2O_3 particles was further improved. When the sintering temperature is 500°C, sharp strong peaks corresponding to Sb_2O_3 and SnO_2 can be seen, respectively. Meanwhile, the intensity of characteristic peak of SnO_2 is weaker than that of Sb_2O_3, which is also confirmed that the inner core is SnO_2 wrapped with Sb_2O_3 shell. The Raman spectroscopy was used to determine the presence of carbon in SnO_2@C@Sb_2O_3. The spectrum of **Figure 4B** clearly shows the characteristic peaks of D and G band located at 1,342 and 1,590 cm^{-1}, respectively, which corresponding to typical in-plane vibration of sp^2-bonded carbon atoms and vibrational modes from sp^3-bonded carbon atoms in amorphous carbon (Sevilla and Fuertes, 2009). The peak intensity ratio (I_D/I_G) is 1.03, indicating that the carbon in SnO_2@C@Sb_2O_3 is highly disordered, which is conducive to improving the electrochemical activity of electrode materials (Sun et al., 2019; Qin et al., 2020).

XPS measurements were carried out to further examine the composition of elements and chemical bonding states in the SnO_2@C@Sb_2O_3. The survey spectra of **Figure 4C** can clearly observe the corresponding peaks of C, Sn, Sb, and O. The valence states of Sn and Sb can be further analyzed by XPS, as shown in **Figure 4D**. The high-resolution Sn 3d XPS spectrum shows that peaks located at 486.43 and 494.84 eV correspond to Sn $3d_{5/2}$ and Sn $3d_{3/2}$ of SnO_2, respectively (Lee et al., 2017). The Sb 3d XPS spectrum comprises two peaks, located at 530.29 and 539.57 eV, respectively, which correspond to $3d_{5/2}$ and $3d_{3/2}$ of Sb_2O_3 (Wang et al., 2017).

Figure 5 is the formation process of fabricating multi-metal oxides and carbon composites with multilayer core/shell hollow structure. First, the nanoparticles of Sn^{4+}, glucose, and Sb^{3+} core/shell structure with surface functional groups were prepared. Then, the uniform metal oxide hydrate core/shell structure with carbonaceous interlayer as precursors was formed by a hydrothermal reaction. Previous studies have shown that carbon-rich polysaccharides can be carbonized by sintering at lower temperatures, and that the glucose can be converted into carbon-rich polysaccharide by hydrothermal process (Zhao et al., 2010). Subsequently, SnO_2@C@Sb_2O_3 multilayer core–shell submicrospheres were sintered at different temperatures. With the increasing of the annealing temperature from 300 to 400°C, the surface of solid spheres has been shrunk to form a stable metal oxide shell with a smooth surface because the crystallization of the metal oxide hydrate accelerates, and the carbonaceous layer has also been formed. At a higher annealing temperature, because the combustion of carbonaceous intermediate layer causes the oxide of shell and core to shrink, it provides energy for the phase separation between shell and core, so the hollow effect appears (Zheng et al., 2009). Thus, this syntheses method of SnO_2@C@Sb_2O_3 multilayer hollow spheres is promoting to form various multilayer metal oxides within the carbonaceous interlayer.

Figure 6 is the electrochemical performances of the SnO_2@C@Sb_2O_3 composite as anode for SIBs. The charge–discharge curve of the SnO_2@C@Sb_2O_3 electrode at the current density of 1,500 mA g^{-1} is shown in **Figure 6A**. The initial discharge and charging capacity are 476 and 395, respectively. The initial Coulomb efficiency (ICE) is as high as 82.9%, which is attributed to the ease and efficiency of ion/electron transport in the porous shell sphere (Zhang et al., 2015). **Figure 6B** is the discharge–charge voltage profile of SnO_2@C@Sb_2O_3 at 0.1 mV s^{-1}. The first cycle shows a strong reduction peak at 0.5 V which disappears in the following cycles, indicating that there is an irreversible reaction to form electrolyte interphase (SEI) film during the first discharge process. In subsequent cathodic scans, three reduction peaks appeared between 0.01 and 1.0 V, which was related to the reaction of Na^+ with SnO_2 and Sb_2O_3 to form Sn, Sb, Na_xSn ($x \leq 3.75$), and Na_ySb ($y \leq 3$) (Jahel et al., 2015; Kim et al., 2019). Moreover, the two oxidation peaks were about 0.72 and 0.85 V, respectively, corresponding to the de-alloying reactions of Na_xSn and Na_ySb. After the first cycle, the overlap CV curves for subsequent cycles indicate the good stability and reversibility of the as-prepared submicrospheres. The discharge capacities of SnO_2@C@Sb_2O_3 anode after 100 cycles at current densities of 150 and 1,500 mA g^{-1} are 423 and 269 mAh g^{-1}, respectively, as shown in **Figure 6C**. The excellent cycling performance of the SnO_2@C@Sb_2O_3 electrode is attributing to the carbon interlayer and the hollow layer absorb the mechanical stress caused by the volume expansion of SnO_2 and Sb_2O_3, which is related to the structural integrity. Interestingly, the charge–discharge capacity showed a downward trend and then an upward trend, indicating that the electrode has an activation process in the cycle. In the initial stage, the inside of the SnO_2@C@Sb_2O_3 electrode is

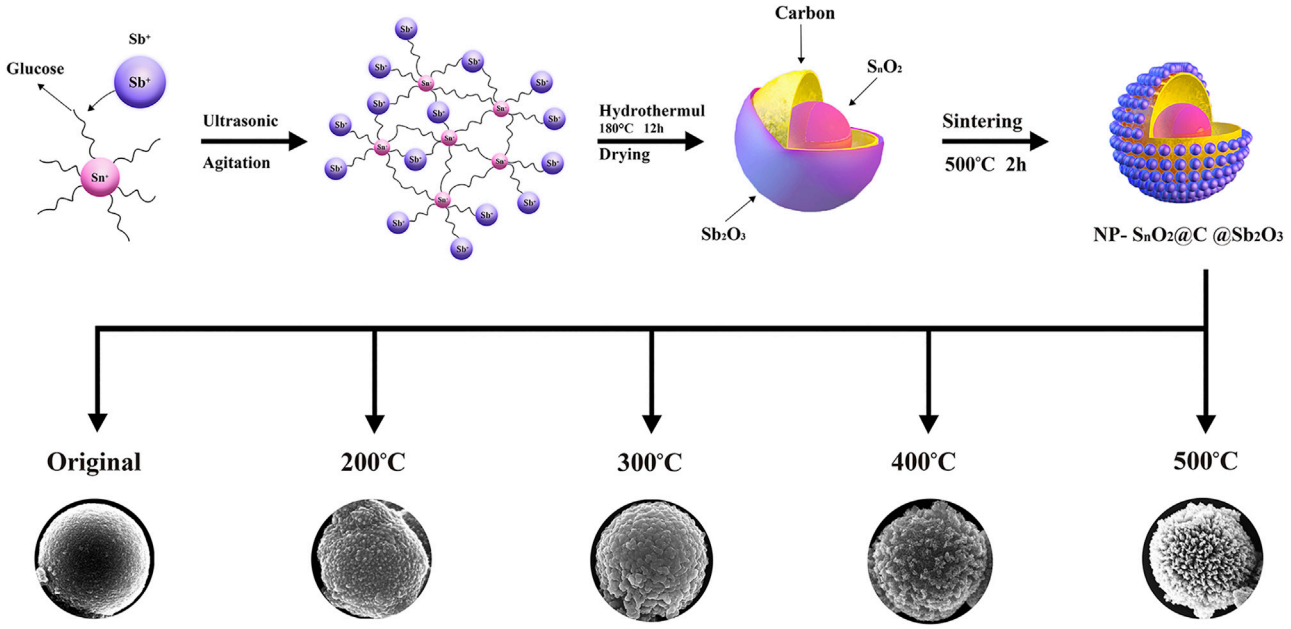

FIGURE 5 | Schematic of SnO_2@C@Sb_2O_3 core–shell mesoporous spheres.

difficult to be wetted by the electrolyte, but the outer shell is more likely to come into contact with sodium ions and react. After the charging–discharging process lasts for a period of time, the electrode can be completely soaked by the electrolyte (Sun et al., 2014). The rate performance of the SnO_2@C@Sb_2O_3 anode is shown in **Figure 6D**. It delivers the specific discharge capacities of 427, 397, 360, and 308 mAh g^{-1} at the current densities of 150, 300, 600, and 1,200 mA g^{-1}, respectively. When back to 150 mA g^{-1}, the capacity can retain back to 390 mAh g^{-1}, which exhibited the excellent rate electrochemical performance. The cycling performance and rate performance of SnO_2 and Sb_2O_3 as SIB anodes are shown in **Figures 6E,F**. Obviously, SnO_2 and Sb_2O_3 anodes exhibit rapid capacity degradation during cycling and poor rate performance compared to SnO_2@C@Sb_2O_3. The electrochemical performance of SnO_2@C@Sb_2O_3 as SIB anode is compared with other metal oxide anodes previously reported in **Table 1**. It is obvious that SnO_2@C@Sb_2O_3 anodes have better cycling and rate performance. The *ex situ* XRD shown in **Figure 7** illustrates the changes in the composition of the anode during the first charge/discharge. Several diffraction peaks of $Na_{3.75}Sn$ and Na_3Sb are observed at the SnO_2@C@Sb_2O_3 anode during full discharge, indicating that Na^+ were embedded in the anode material. When fully charged, the diffraction peaks of the corresponding $Na_{3.75}Sn$ and Na_3Sb basically disappeared, while the peaks of SnO_2@C@Sb_2O_3 strengthened, indicating that Na^+ was extracted from the anode (Nam et al., 2015; Bian et al., 2016). This is consistent with the analysis results in **Figure 6B**.

The higher rate property and excellent cycling life of SnO_2@C@Sb_2O_3 for SIBs are due to the multilayer core–shell nanostructures and the multi-compositions. The working mechanism of SnO_2@C@Sb_2O_3 as the anode of SIBs is shown in **Figure 8**. The surface of the submicrospheres with multilayer core–shell structure is most likely to contact and react with the electrolyte, and the core can fully contact with the electrolyte after several cycles, which is an activation process (Zu et al., 2017; Sarkar et al., 2019; Zhang et al., 2019; Qin et al., 2020). Therefore, the cycle curve of SnO_2@C@Sb_2O_3 anode shows a trend of first decreasing and then increasing. Then, the carbon as the interlayer structure from glucose could improve the electric conductivity of the electrode effectively and shorten the electron transport pathway. At the same time, the hollow core of SnO_2 and the carbon layer can accommodate the volume expansion caused by the alloy reaction. Furthermore, the synergistic effects of the multi-compositions (SnO_2 and Sb_2O_3) could enhance electrochemical activities over the single metal oxide nanocomposite. Finally, the multilayer core–shell structure and hollow structure could buffer partially the dramatic volume of SnO_2 and Sb_2O_3 during the sodiation/disodiation process. Benefited from both structure effect and synergistic effect of the nanocomposite materials with special structure, the good cycle performance and high rate capability are achieved by SnO_2@C@Sb_2O_3 anode for SIBs.

CONCLUSION

Based on hydrothermal method and high temperature carbonization, SnO_2@C@Sb_2O_3 composites with multilayer hollow core–shell structure were prepared. The multilayers hollow core–shell structure effectively cushioned the volume expansion of the inner oxide and maintained the integrity of the overall volume. The carbon layer provides excellent electron channel and improves the efficiency of electron transport. Meanwhile, the

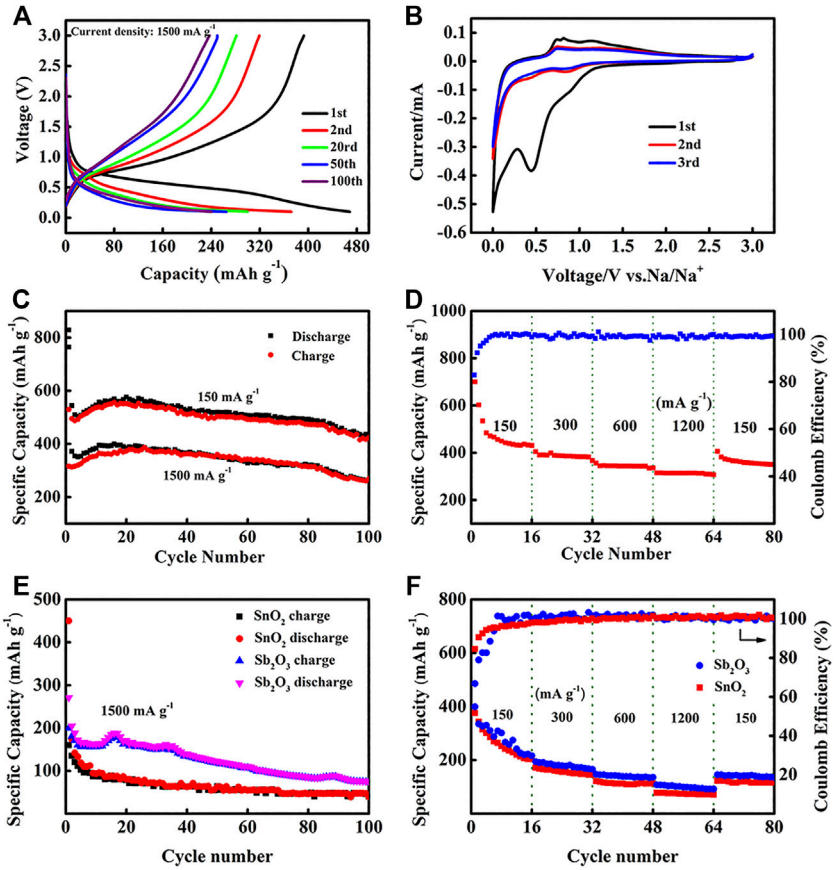

FIGURE 6 | Electrochemical performance of SnO_2@C@Sb_2O_3 for SIBs in the voltage range of 0.01–3.0 V (vs. Na/Na^+). **(A)** The selected discharge–charge curves at 1,500 mA g^{-1}, **(B)** CV curves at the sweep rate of 0.1 mV s^{-1}, **(C)** cycling performance at 150 and 1,500 mA g^{-1}, **(D)** rate performance of SnO_2@C@Sb_2O_3 anode, **(E)** cycling performance of SnO_2 and Sb_2O_3 anode at 1,500 mA g^{-1}, and **(F)** rate performance of SnO_2 and Sb_2O_3 anode.

TABLE 1 | Comparison of electrochemical performance among reported metal oxide electrode materials.

Typical materials	Initial Coulomb efficiency (%)	Remain capacity (mAh g^{-1})	Rate properties (mAh g^{-1})	Reference
Sb_2O_3 nanowires	~36	143 (20 mA g^{-1}; 30 cycles)	Not reported	Li et al. (2014)
SnO_2@graphene	~31	~300 (160 mA g^{-1}; 100 cycles)	508 (0.08 A g^{-1}) 302 (0.16 A g^{-1}) 262 (0.32 A g^{-1})	Su et al. (2013a)
CuO/Cu	61.3	320 (100 mA g^{-1}; 100 cycles)	278 (0.3 A g^{-1}) 231 (0.5 A g^{-1}) 165 (1 A g^{-1})	Zheng et al. (2018)
MoO_2/GO	81	389 (100 mA g^{-1}; 100 cycles)	346 (0.2 A g^{-1}) 223 (0.5 A g^{-1}) 140 (1 A g^{-1})	Huang et al. (2015)
SnO_2@C@Sb_2O_3	82.9	423 (150 mA g^{-1}; 100 cycles) 269 (1.5 A g^{-1}; 100 cycles)	397 (0.3 A g^{-1}) 360 (0.6 A g^{-1}) 308 (1.2 A g^{-1})	Our work

outer and inner oxides crystallize better after high sintering, and the synergistic effect between Sb_2O_3 and SnO_2 improves the performance stability. As an anode for SIBs, it can deliver an initial discharge capacity of 476 mAh g^{-1} at a high current density of 1,500 mA g^{-1} and a Coulomb efficiency of 82.9%. After 100 cycles, the discharge capacities of the as-prepared composite are 423 and 269 mAh g^{-1} at 150 and 1,500 mA g^{-1}, respectively. This research gives a rational direction for designing the core–shell composite transition metal oxide materials to improve the performance of sodium-ion batteries.

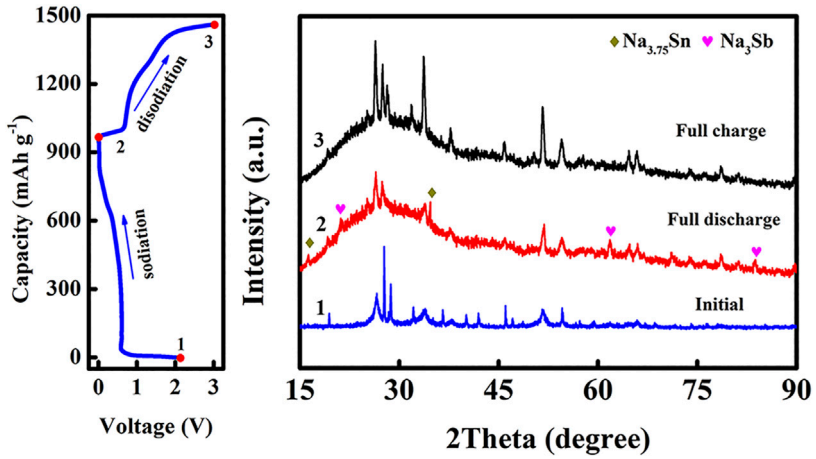

FIGURE 7 | Typical initial charge/discharge profile and the corresponding *ex situ* XRD patterns at various states.

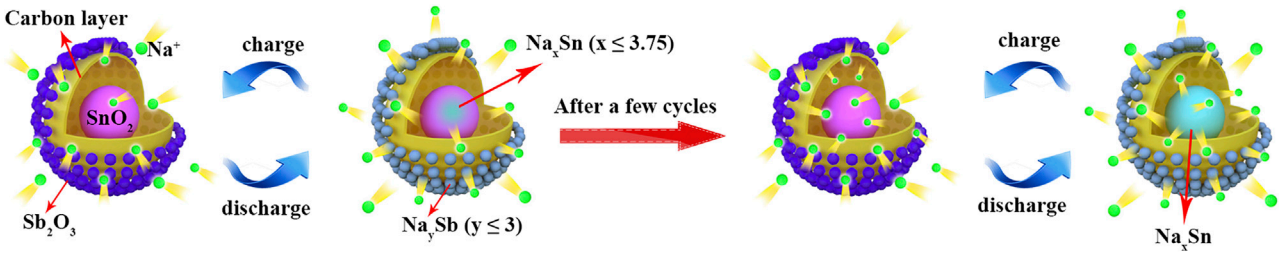

FIGURE 8 | Schematic illustration of charging–discharging characteristics of SnO_2@C@Sb_2O_3 as anode materials for SIBs.

DATA AVAILABILITY STATEMENT

The original contributions presented in the study are included in the article/Supplementary Material, and further inquiries can be directed to the corresponding authors.

AUTHOR CONTRIBUTIONS

GZ synthesized SnO_2@C@Sb_2O_3 composites, did the material characterization, did the electrochemical performance test and data analysis process, and wrote the manuscript. YQ supported for writing the manuscript. LW and LD designed the experimental scheme, analyzed and discussed the experimental data, and wrote the article. JY and YZ provided some help with this experiment. All authors contributed to the article and approved submitted version.

FUNDING

This work was supported by the National Nature Science Foundation of China (Grant No. 61774022) and 2020 Li Ka Shing Foundation Cross-Disciplinary Research Grant (Project No. 2020LKSFG01A).

REFERENCES

Bang, B. M., Lee, J.-I., Kim, H., Cho, J., and Park, S. (2012). High-performance macroporous bulk silicon anodes synthesized by template-free chemical etching. *Adv. Energy Mater.* 2, 878–883. doi:10.1002/aenm.201100765

Bian, H., Zhang, J., Yuen, M.-F., Kang, W., Zhan, Y., Yu, D. Y. W., et al. (2016). Anodic nanoporous SnO_2 grown on Cu foils as superior binder-free Na-ion battery anodes. *J. Power Sources* 307, 634–640. doi:10.1016/j.jpowsour.2015.12.118

Chen, J., Jiang, S., Liu, Y.-R., Huang, T., Wang, C.-Y., Miao, S.-K., et al. (2017). Interaction of oxalic acid with dimethylamine and its atmospheric implications. *RSC Adv.* 7, 6374–6388. doi:10.1039/c6ra27945g

Dong, S., Li, C., Li, Z., Zhang, L., and Yin, L. (2018). Mesoporous hollow Sb/ZnS@C core-shell heterostructures as anodes for high-performance sodium-ion batteries. *Small* 14, e1704517. doi:10.1002/smll.201704517

Eguia-Barrio, A., Castillo-Martinez, E., Liu, X., Dronskowski, R., Lezama, L., Armand, M., et al. (2017). Advanced anode materials for sodium ion batteries: carbodiimides. *MRS Adv.* 2, 1165–1176. doi:10.1557/adv.2017.267

Huang, J., Xu, Z., Cao, L., Zhang, Q., Ouyang, H., and Li, J. (2015). Tailoring MoO2/graphene oxide nanostructures for stable, high-density sodium-ion battery anodes. *Energy Technol.* 3, 1108–1114. doi:10.1002/ente.201500160

Jahel, A., Ghimbeu, C. M., Darwiche, A., Vidal, L., Hajjar-Garreau, S., Vix-Guterl, C., et al. (2015). Exceptionally highly performing Na-ion battery anode using

crystalline SnO_2 nanoparticles confined in mesoporous carbon. *J. Mater. Chem. A* 3, 11960–11969. doi:10.1039/c5ta01963j

Kim, S., Qu, S., Zhang, R., and Braun, P. V. (2019). High volumetric and gravimetric capacity electrodeposited mesostructured Sb_2 O_3 sodium ion battery anodes. *Small* 15, e1900258. doi:10.1002/smll.201900258

Kim, S.-W., Seo, D.-H., Ma, X., Ceder, G., and Kang, K. (2012). Electrode materials for rechargeable sodium-ion batteries: potential alternatives to current lithium-ion batteries. *Adv. Energy Mater.* 2, 710–721. doi:10.1002/aenm.201200026

Lee, J.-I., Song, J., Cha, Y., Fu, S., Zhu, C., Li, X., et al. (2017). Multifunctional SnO2/3D graphene hybrid materials for sodium-ion and lithium-ion batteries with excellent rate capability and long cycle life. *Nano Res.* 10, 4398–4414. doi:10.1007/s12274-017-1756-3

Lee, S. H., Noh, Y., Jo, Y.-R., Kim, Y., Kim, B.-J., and Kim, W. B. (2018). Carbon-encapsulated SnO_2 core-shell nanowires directly grown on reduced graphene oxide sheets for high-performance Li-ion battery electrodes. *Energy Technol.* 6, 1255–1260. doi:10.1002/ente.201700804

Li, K., Liu, H., and Wang, G. (2014). Sb_2O_3 nanowires as anode material for sodium-ion battery. *Arab. J. Sci. Eng.* 39, 6589–6593. doi:10.1007/s13369-014-1194-4

Liu, J., Hartono, S. B., Jin, Y. G., Li, Z., Lu, G. Q., and Qiao, S. Z. (2010). A facile vesicle template route to multi-shelled mesoporous silica hollow nanospheres. *J. Mater. Chem.* 20, 4595–4601. doi:10.1039/b925201k

Luo, W., Shen, F., Bommier, C., Zhu, H., Ji, X., and Hu, L. (2016). Na-ion battery anodes: materials and electrochemistry. *Acc. Chem. Res.* 49, 231–240. doi:10.1021/acs.accounts.5b00482

Ma, W., Liu, X., Wang, X., Wang, Z., Zhang, R., Yuan, Z., et al. (2016). Crystalline Cu-silicide stabilizes the performance of a high capacity Si-based Li-ion battery anode. *J. Mater. Chem. A* 4, 19140–19146. doi:10.1039/c6ta08740j

Morita, K., Okamoto, N., Fujiyama, T., Saito, T., and Kondo, K. (2016). Sn negative electrode consists of amorphous structures for sodium ion secondary batteries. *MRS Adv.* 1, 409–414. doi:10.1557/adv.2016.117

Nam, D. H., Hong, K. S., Lim, S. J., Kim, M. J., and Kwon, H. S. (2015). High-performance Sb/Sb_2O_3 anode materials using a polypyrrole nanowire network for Na-ion batteries. *Small* 11, 2885–2892. doi:10.1002/smll.201500491

Qin, Y., Zhang, Y., Wang, J., Zhang, J., Zhai, Y., Wang, H., et al. (2020). Heterogeneous structured Bi_2S_3/MoS_2@NC nanoclusters: exploring the superior rate performance in sodium/potassium ion batteries. *ACS Appl. Mater. Interfaces* 12, 42902–42910. doi:10.1021/acsami.0c13070

Rui, X., Yan, Q., Skyllas-Kazacos, M., and Lim, T. M. (2014). $Li_3V_2(PO_4)_3$ cathode materials for lithium-ion batteries: a review. *J. Power Sources* 258, 19–38. doi:10.1016/j.jpowsour.2014.01.126

Sarkar, A., Sinha, A. K., and Mitra, S. (2019). Nanostructured vanadium tri-oxides, as a long life and high performance anode for sodium-ion battery. *Electrochim. Acta* 299, 914–925. doi:10.1016/j.electacta.2019.01.076

Sevilla, M., and Fuertes, A. B. (2009). The production of carbon materials by hydrothermal carbonization of cellulose. *Carbon* 47, 2281–2289. doi:10.1016/j.carbon.2009.04.026

Shan, X., Guo, Z., Zhang, X., Yang, J., and Duan, L. (2019). Mesoporous TiO_2 nanofiber as highly efficient sulfur host for advanced lithium–sulfur batteries. *Chin. J. Mech. Eng.* 32, 60–67. doi:10.1186/s10033-019-0374-2

Su, D., Ahn, H. J., and Wang, G. (2013a). SnO_2@graphene nanocomposites as anode materials for Na-ion batteries with superior electrochemical performance. *Chem. Commun.* 49, 3131–3133. doi:10.1039/c3cc40448j

Su, D., Dou, S., and Wang, G. (2014). WS(2)@graphene nanocomposites as anode materials for Na-ion batteries with enhanced electrochemical performances. *Chem. Commun.* 50, 4192–4195. doi:10.1039/c4cc00840e

Su, D., Wang, C., Ahn, H., and Wang, G. (2013b). Octahedral tin dioxide nanocrystals as high capacity anode materials for Na-ion batteries. *Phys. Chem. Chem. Phys.* 15, 12543–12550. doi:10.1039/c3cp52037d

Sun, H., Xin, G., Hu, T., Yu, M., Shao, D., Sun, X., et al. (2014). High-rate lithiation-induced reactivation of mesoporous hollow spheres for long-lived lithium-ion batteries. *Nat. Commun.* 5, 4526. doi:10.1038/ncomms5526

Sun, Q., Li, D., Cheng, J., Dai, L., Guo, J., Liang, Z., et al. (2019). Nitrogen-doped carbon derived from pre-oxidized pitch for surface dominated potassium-ion storage. *Carbon* 155, 601–610. doi:10.1016/j.carbon.2019.08.059

Sun, X., Liu, J., and Li, Y. (2006). Oxides@C core-shell nanostructures: one-pot synthesis, rational conversion, and Li storage property. *J. Chem. Mater.* 18, 3486–3494. doi:10.1021/cm052648m

Tarascon, J. M., and Armand, M. (2001). Issues and challenges facing rechargeable lithium batteries. *Nature* 414, 359–367. doi:10.1038/35104644

Wang, J. W., Liu, X. H., Mao, S. X., and Huang, J. Y. (2012). Microstructural evolution of tin nanoparticles during *in situ* sodium insertion and extraction. *Nano Lett.* 12, 5897–5902. doi:10.1021/nl303305c

Wang, Y., Ma, Z., and Lu, C. (2016). A twins-structural Sn@C core–shell composite as anode materials for lithium-ion batteries. *Compos. Interface* 23, 273–280. doi:10.1080/09276440.2016.1136523

Wang, Y.-X., Lim, Y.-G., Park, M.-S., Chou, S.-L., Kim, J. H., Liu, H.-K., et al. (2014). Ultrafine SnO_2 nanoparticle loading onto reduced graphene oxide as anodes for sodium-ion batteries with superior rate and cycling performances. *J. Mater. Chem. A* 2, 529–534. doi:10.1039/c3ta13592f

Wang, Z., Cheng, Y., Li, Q., Chang, L., and Wang, L. (2017). Facile synthesis of one-dimensional hollow Sb_2O_3@TiO_2 composites as anode materials for lithium ion batteries. *J. Power Sources* 389, 214–221. doi:10.1016/j.jpowsour.2018.04.013

Wu, L., Hu, X., Qian, J., Pei, F., Wu, F., Mao, R., et al. (2013). A Sn–SnS–C nanocomposite as anode host materials for Na-ion batteries. *J. Mater. Chem. A* 1, 7181–7184. doi:10.1039/c3ta10920h

Xu, C., Hao, Q., and Zhao, D. (2016). Facile fabrication of a nanoporous Si/Cu composite and its application as a high-performance anode in lithium-ion batteries. *Nano Res.* 9, 908–916. doi:10.1007/s12274-015-0973-x

Zhang, F., Yang, C., Gao, X., Chen, S., Hu, Y., Guan, H., et al. (2017). SnO_2@PANI core-shell nanorod arrays on 3D graphite foam: a high-performance integrated electrode for lithium-ion batteries. *ACS Appl. Mater. Interfaces* 9, 9620–9629. doi:10.1021/acsami.6b15880

Zhang, Y., Tao, H., Du, S., and Yang, X. (2019). Conversion of MoS_2 to a ternary MoS_2-xSe x alloy for high-performance sodium-ion batteries. *ACS Appl. Mater. Interfaces* 11, 11327–11337. doi:10.1021/acsami.8b19701

Zhang, Y., Zhu, P., Huang, L., Xie, J., Zhang, S., Cao, G., et al. (2015). Few-layered SnS_2 on few-layered reduced graphene oxide as Na-ion battery anode with ultralong cycle life and superior rate capability. *Adv. Funct. Mater.* 25, 481–489. doi:10.1002/adfm.201402833

Zhao, N. H., Yang, L. C., Zhang, P., Wang, G. J., Wang, B., Yao, B. D., et al. (2010). Polycrystalline SnO_2 nanowires coated with amorphous carbon nanotube as anode material for lithium ion batteries. *Mater. Lett.* 64, 972–975. doi:10.1016/j.matlet.2010.01.077

Zheng, M., Liu, Y., Xiao, Y., Zhu, Y., Guan, Q., Yuan, D., et al. (2009). An easy catalyst-free hydrothermal method to prepare monodisperse carbon microspheres on a large scale. *J. Phys. Chem. C* 113, 8455–8459. doi:10.1021/jp811356a

Zheng, T., Li, G., Li, D., and Meng, X. (2018). Based on Cu as framework constructed nanoporous CuO/Cu composites by a dealloy method for sodium-ion battery anode. *J. Nanopart. Res.* 20, 140. doi:10.1007/s11051-018-4245-z

Zhu, H., Jia, Z., Chen, Y., Weadock, N., Wan, J., Vaaland, O., et al. (2013). Tin anode for sodium-ion batteries using natural wood fiber as a mechanical buffer and electrolyte reservoir. *Nano Lett.* 13, 3093–3100. doi:10.1021/nl400998t

Zu, L., Su, Q., Zhu, F., Chen, B., Lu, H., Peng, C., et al. (2017). Antipulverization electrode based on low-carbon triple-shelled superstructures for lithium-ion batteries. *Adv. Mater.* 29, 1701494. doi:10.1002/adma.201701494

Conflict of Interest: The authors declare that the research was conducted in the absence of any commercial or financial relationships that could be construed as a potential conflict of interest.